Accurate and efficient prediction of the band gaps and optical spectra of chalcopyrite semiconductors from a nonempirical range-separated dielectric-dependent hybrid: Comparison with many-body perturbation theory

Arghya Ghosh,[1] Subrata Jana,[2,*] Dimple Rani,[3] Manoar Hossain,[4] Manish K. Niranjan,[1] and Prasanjit Samal[3]

[1]*Department of Physics, Indian Institute of Technology, Hyderabad, India*

[2]*Department of Molecular Chemistry and Materials Science, Weizmann Institute of Science, Rehovoth 76100, Israel*

[3]*School of Physical Sciences, National Institute of Science Education and Research, An OCC of Homi Bhabha National Institute, Jatni, India*

[4]*Institut für Physik and IRIS Adlershof, Humboldt-Universität zu Berlin, Zum Großen Windkanal 2, 12489 Berlin, Germany*

(Received 23 November 2023; revised 25 December 2023; accepted 3 January 2024; published 17 January 2024)

The accurate prediction of electronic and optical properties in chalcopyrite semiconductors has been a persistent challenge for density-functional-theory (DFT) -based approaches. Addressing this issue, we demonstrate that very accurate results can be obtained using a nonempirical screened dielectric-dependent hybrid (DDH) functional. This approach showcases its impressive capability to accurately determine band gaps, optical bowing parameters, and optical-absorption spectra for chalcopyrite systems. What sets the screened DDH functional apart is its adeptness in capturing the many-body physics associated with highly localized *d* electrons. Notably, the accuracy is comparable to the many-body perturbation-based methods (such as G_0W_0 or its various approximations for band gaps and the Bethe-Salpeter equation on the top of the G_0W_0 or its various approximations for optical spectra) with less computational cost, ensuring a more accessible application across various research domains. The present results show the predictive power of the screened DDH functional, pointing toward promising applications where computational efficiency and predictive accuracy are crucial considerations. Overall, the screened DDH functional offers a compelling balance between cost-effectiveness and precision, making it a valuable tool for future endeavors in exploring chalcopyrite semiconductors and beyond.

DOI: 10.1103/PhysRevB.109.045133

I. INTRODUCTION

Over the past two decades, ternary chalcopyrite semiconductors have attracted a great deal of attention due to their applications in renewable and sustainable technologies [1–6]. In particular, these materials are primarily used as absorbers in thin film solar cells due to their great off-stoichiometric steadiness [7], tunable electrical and thermal conductivity [8], and remarkable optoelectronic characteristics [5]. The presence of heavy metals (Cu, Ag, Be, etc.), coupled with their tunable electronic structure, adds an intriguing dimension from a scientific perspective. The *ab initio* calculations for these ternary chalcopyrite semiconductors, characterized by a complex electronic structure, are essential and have been of prime importance. However, the *ab initio* calculations have long predicted that the band gap will be strongly influenced by the anion displacement (u) from its primary mean position [9,10].

Experimentally, acquiring the band gaps and optical spectra of Cu and Ag chalcopyrite systems typically involves techniques such as photoemission or photoluminescence spectra [6,11–13]. However, from a theoretical standpoint, achieving an accurate treatment of excited states in these systems requires a comprehensive approach. This often involves either a fully relativistic treatment of many-body perturbation theory (MBPT) or a fully self-consistent Green function-based method (GW) [14,15] accompanied by the solution of the Bethe-Salpeter equation (BSE) [16]. While approaches such as fully self-consistent GW and BSE@GW encompass crucial many-body effects, such as electron-electron (e-e) and electron-hole (e-h) interactions [15,17–19], they are known to be computationally demanding and technically challenging, posing significant hurdles to their widespread application.

Importantly, there are several limitations when higher-level methods are applied to study the electronic structure of chalcopyrite systems. First, the strong p-d hybridization near the top of the valence band closes the Kohn-Sham (KS) band gap, causing a divergence in the dipole transition matrix element, which poses a significant challenge in constructing a reliable response function in GW or BSE@GW calculations. Consequently, these higher-level methods depend strongly on the chosen density functional theory (DFT) wave functions and orbital energies, and an inaccurate estimation of the dielectric function may lead to wrong exciton effects [20,21]. Secondly, the band gaps of chalcopyrite systems depend crucially on the parameters related to the crystal structure, particularly on anion displacement (u) [9,21]. Thus, an incorrect estimation of the structural parameters can affect the excitonic wave function. Consequently, due to these factors, unphysical absorption peaks may appear in the *ab initio* optical spectrum.

*Corresponding author: subrata.niser@gmail.com

Nevertheless, there is an emerging alternative method for tackling inherently complex issues related to excited-state electronic properties. This novel method is based on the solution to the KS equation or a generalized KS scheme using the dielectric-dependent hybrid functional (DDH) [22–26]. In this paper, we employ dielectric-dependent hybrid functionals to investigate the electronic structure and optical properties of chalcopyrite semiconductors. The DDH functional scheme is proposed as a viable alternative to the highly demanding and complex *GW* and BSE@*GW* schemes, offering a more accessible approach for exploring various systems [23–37]. Notably, to the best of our knowledge, no study has been reported on the performance of the DDH functional in the case of ternary chalcopyrite semiconductors.

The findings presented in our work strongly suggest the efficacy of the DDH functional as a state-of-the-art scheme for accurately characterizing both ground-state and excited-state electronic properties in highly localized d electronic systems, particularly within the chalcopyrite framework where describing the robust hybridization between p and d orbitals is crucial. While modern meta-generalized gradient approximations outperform generalized gradient approximations (GGAs) in terms of structural and band-gap properties of semiconductors [38–44], they are plagued by well-known issues such as many-electron self-interaction and delocalization errors [45–48], sometimes inadequate in capturing the degree of electron correlation [49–51].

This paper evaluates the accuracy of the nonempirical screened DDH functional in predicting band gaps and optical absorption spectra of chalcopyrite semiconductors. Our results indicate that screened-DDH, addressing the generalized KS scheme, agrees reasonably well with experimental findings for both band gaps and optical spectra. Notably, the functional is particularly effective for challenging Cu-based chalcopyrites. Our calculations demonstrate the applicability of this method in describing the *p-d* hybridization where other high-level methods are either insufficient or computationally demanding.

II. BACKGROUND OF METHODOLOGIES

The Coulomb attenuated method (CAM) of the two-electron operator is used to construct the screened range-separated hybrid (SRSH) as [36]

$$\frac{1}{r_{ij}} = \frac{\alpha + \beta\,\mathrm{erf}(\mu r_{ij})}{r_{ij}} + \frac{1 - [\alpha + \beta\,\mathrm{erf}(\mu r_{ij})]}{r_{ij}}, \quad (1)$$

where $r_{ij} = |\mathbf{r}_i - \mathbf{r}_j|$ is the relative position of two electrons. Here, $0 \leqslant \alpha \leqslant 1$ and $0 \leqslant \beta \leqslant 1$ control the amounts of Fock (nonlocal) and semilocal (sl) GGA [Perdew-Burke-Ernzerhof (PBE) in this case] [52] that are mixed to the full exchange-correlation (XC) functional in its long range (lr) or short range (sr). μ is the screening parameter determined later in this paper. Using Eq. (1), the resultant generalized form of the SRSH XC expression becomes

$$\begin{aligned} E_{\mathrm{xc}}^{\mathrm{SRSH}}(\alpha,\beta;\mu) = {} & (1-\alpha)E_x^{\text{sr-sl},\mu} + \alpha E_x^{\text{Fock-sr},\mu} \\ & + [1-(\alpha+\beta)]E_x^{\text{sl-lr},\mu} \\ & + (\alpha+\beta)E_x^{\text{Fock-lr},\mu} + E_c^{\mathrm{sl}} \end{aligned} \quad (2)$$

and the corresponding potential is

$$\begin{aligned} V_{\mathrm{xc}}^{\mathrm{SRSH}}(\alpha,\beta;\mu) = {} & [\alpha + \beta\,\mathrm{erf}(\mu r)]V_x^{\mathrm{Fock}} + \beta V_x^{\text{sl-sr},\mu} \\ & + [1-(\alpha+\beta)]V_x^{\mathrm{sl}} + V_c^{\mathrm{sl}}. \end{aligned} \quad (3)$$

Here, E_c and V_c are the PBE correction energy and potential functionals, respectively. Equation (3) can be seen as the generalized form of the "CAM"-type hybrid used extensively for finite and extended systems [23–37]. However, the naming of the functionals becomes different based on how one determines the parameters. Typically, one can consider $\alpha + \beta = \gamma$, where γ is an another parameter. In terms of α and γ, Eq. (3) becomes

$$\begin{aligned} V_{\mathrm{xc}}^{\mathrm{SRSH}}(\alpha,\gamma;\mu) = {} & [\alpha - (\alpha-\gamma)\mathrm{erf}(\mu r)]V_x^{\mathrm{Fock}} \\ & - (\alpha-\gamma)V_x^{\text{sl-sr},\mu} + (1-\gamma)V_x^{\mathrm{sl}} + V_c^{\mathrm{sl}}. \end{aligned} \quad (4)$$

In particular, the following choices are important for bulk solids: (i) for $\alpha = 0.25$, $\gamma = 0$, and $\mu = 0.11$ Bohr^{-1} in Eq. (4), resulting in the recovery of the HSE06-like functionals [53–60],

$$\begin{aligned} V_{\mathrm{xc}}^{\mathrm{HSE06}}(0.25,0;0.11) = {} & 0.25[1-\mathrm{erf}(0.11r)]V_x^{\mathrm{Fock}} \\ & - 0.25V_x^{\text{sl-sr},0.11} + V_x^{\mathrm{sl}} + V_c^{\mathrm{sl}}. \end{aligned} \quad (5)$$

(ii) For $\alpha = 1$ and $\gamma = \varepsilon_\infty^{-1}$, where ε_∞ is the high-frequency macroscopic static dielectric constant, the ion-clamped static (optical) dielectric constant, or the electronic dielectric constant, the resultant functional becomes

$$\begin{aligned} V_{\mathrm{xc}}^{\mathrm{DDH}}\big(1,\varepsilon_\infty^{-1};\mu\big) = {} & \big[1-\big(1-\varepsilon_\infty^{-1}\big)\mathrm{erf}(\mu r)\big]V_x^{\mathrm{Fock}} \\ & - \big(1-\varepsilon_\infty^{-1}\big)V_x^{\text{sl-sr},\mu} + \big(1-\varepsilon_\infty^{-1}\big)V_x^{\mathrm{sl}} + V_c^{\mathrm{sl}}, \end{aligned} \quad (6)$$

which is named the dielectric-dependent range-separated hybrid functional based on the CAM (DD-RSH-CAM) [23] or simply DDH (used throughout this paper).

In particular, the model dielectric function for bulk solid is defined according to Eq. (4) with $\gamma = \varepsilon_\infty^{-1}$ as

$$\varepsilon^{-1}(|\mathbf{G}|) = \alpha - \big(\alpha - \varepsilon_\infty^{-1}\big)e^{-|\mathbf{G}|^2/(4\mu)}, \quad (7)$$

which is the key to the DDH functional (where $\mathbf{G}$ is the reciprocal-lattice vector). The model dielectric function makes this construction quite similar to that of the self-energy correction of *GW*, in particular when GGA approximates $\sum_{\mathrm{COH}}$ [Coulomb hole (COH)] and $\sum_{\mathrm{SEX}}$ [screened exchange (SEX)] by the Fock term [61].

It is readily apparent from Eq. (6) that the macroscopic static dielectric constant, ε_∞, is the key to DDH calculations. It can be obtained using different procedures discussed in Sec. III B. Several procedures are also available to determine the screening parameter μ. In particular, μ can be obtained (i) depending on the valance electron density that participates in the screening [22,61,62], (ii) from fitting with the accurate dielectric function [23], (iii) from empirical fitting [63], or (iv) from a first-principles method using linear-response TDDFT (LR-TDDFT) approaches based on local density or local Seitz radius (r_s) [26]. In particular, in this paper we use procedure (iv) to determine μ, which is named $\mu_{\mathrm{eff}}^{\mathrm{fit}}$ and obtained using

the compressibility sum rule together with LR-TDDFT [26], which has the form

$$\mu = \mu_{\text{eff}}^{\text{fit}} = \frac{a_1}{\langle r_s \rangle} + \frac{a_2 \langle r_s \rangle}{1 + a_3 \langle r_s \rangle^2}, \tag{8}$$

with $a_1 = 1.917\,18$, $a_2 = -0.028\,17$, $a_3 = 0.149\,54$, and

$$\langle r_s \rangle = \frac{1}{V_{\text{cell}}} \int_{\text{cell}} \left(\frac{3}{4\pi [n_\uparrow(\mathbf{r}') + n_\downarrow(\mathbf{r}')]} \right)^{1/3} d^3 r'. \tag{9}$$

The readers are referred to Ref. [26] for the details of this formula and underlying derivations. It may be noted that the resultant $\mu_{\text{eff}}^{\text{fit}}$ performs quite similarly to those obtained from the fitting of the dielectric function [23] as reported in Ref. [26]. On the other hand, the screening parameters determined from procedure (i) are not always well-defined in some materials, especially where electrons of different characters participate in the valence bands [64]. In this respect, determining screening parameters from method (iv) is quite reasonable and well justified [26].

In the subsequent discussion, we briefly overview the different levels within the *GW*, which we have used whenever applicable. Various approximations exist for *GW*, including the single-shot G_0W_0 calculation, which relies heavily on the choice of the initial KS wave functions and orbital energies [65]. On the other hand, GW_0 involves a self-consistent update of the orbital energies in the Green's function G after the initial G_0W_0 step [66,67]. One may note the crucial distinctions between *GW* and DDH. The *GW* steps involve the calculations of the frequency-dependent dielectric function, including the summations over both occupied and unoccupied states. This makes the self-consistent update of *GW* computationally more expensive. In contrast, the DDH calculations are performed only within the generalized KS (gKS) scheme. However, it requires an additional calculation of dielectric constants (details are provided in Sec. III C). Second, the outcomes of one-shot G_0W_0 and partially self-consistent GW_0 are highly dependent on the initial choice of the KS functional, while DDH, being a self-consistent approach within gKS, yields outcomes independent of the initial state.

III. RESULTS AND DISCUSSIONS

A. Materials and calculation details

1. Materials

We use 42 chalcopyrite semiconductors having ABX_2 structures (with space group $I\bar{4}2d$) grouped as I-III-VI_2 (18 chalcopyrites) and I-III-VI_2 (24 chalcopyrites), which are the iso-electronic analogs of the II-VI and III-V ideal zinc-blende structure (distorted), respectively [68]. Here, (A, B) are the two cations tetrahedrally coordinated by four anions (X), where each anion is again coordinated by two cations each which are A and B types [69]. Three structural parameters, namely (i) lattice constant a, (ii) tetragonal ratio $\eta = c/2a$, where c is the lattice constant along the z-direction, and (iii) the anion displacement parameter u are used to describe a chalcopyrite structure. Note that u is an important structural parameter used to describe physics related to the interplay between structure and electronic properties, and it is defined as [9]

$$u = 0.25 + \left(r_{A-X}^2 - r_{B-X}^2\right)/a^2, \tag{10}$$

where r_{A-X} and r_{B-X} are $A-X$ and $B-X$ bond lengths, respectively.

DDH, HSE06, and GW_0 band-gap calculations are performed using the PBE optimized geometries. The details of the PBE optimized geometries are given in Table I. In general, the computed lattice constants from PBE XC functionals agree well with the experimental lattice constants.

TABLE I. PBE optimized a (in Å), c, η, r_{A-X} (in Å), r_{B-X} (in Å), and u of all the chalcopyrite semiconductors used in this work.

Solids	a	c	η	r_{A-X}	r_{B-X}	u
			I-III-VI_2			
$AgAlS_2$	5.740	5.251	0.915	2.574	2.277	0.294
$AgAlSe_2$	6.029	5.562	0.922	2.677	2.425	0.285
$AgAlTe_2$	6.409	6.122	0.955	2.812	2.661	0.270
$AgGaS_2$	5.773	5.307	0.919	2.563	2.317	0.286
$AgGaSe_2$	6.049	5.632	0.931	2.665	2.463	0.278
$AgGaTe_2$	6.406	6.169	0.963	2.801	2.681	0.266
$AgInS_2$	5.925	5.749	0.970	2.573	2.509	0.259
$AgInSe_2$	6.195	6.039	0.975	2.673	2.647	0.254
$AgInTe_2$	6.567	6.500	0.990	2.812	2.856	0.244
$CuAlS_2$	5.336	5.274	0.988	2.324	2.28	0.257
$CuAlSe_2$	5.651	5.576	0.987	2.443	2.430	0.252
$CuAlTe_2$	6.094	6.055	0.994	2.603	2.664	0.241
$CuGaS_2$	5.372	5.315	0.989	2.314	2.322	0.249
$CuGaSe_2$	5.677	5.631	0.992	2.432	2.471	0.244
$CuGaTe_2$	6.096	5.086	0.834	2.593	2.685	0.237
$CuInS_2$	5.578	5.617	1.007	2.33	2.519	0.220
$CuInSe_2$	5.871	5.908	1.006	2.447	2.657	0.219
$CuInTe_2$	6.294	6.317	1.003	2.608	2.861	0.215
			II-IV-V_2			
$BeGeAs_2$	5.446	5.48	1.006	2.267	2.468	0.218
$BeGeP_2$	5.207	5.229	1.004	2.177	2.347	0.222
$BeSiAs_2$	5.372	5.368	0.999	2.266	2.388	0.230
$BeSiP_2$	5.129	5.117	0.998	2.166	2.266	0.233
$BeSnAs_2$	5.655	5.697	1.007	2.287	2.650	0.194
$BeSnP_2$	5.428	6.675	1.230	2.198	2.538	0.195
$CdGeAs_2$	6.052	5.746	0.949	2.676	2.485	0.277
$CdGeP_2$	5.805	5.484	0.945	2.583	2.363	0.282
$CdSiAs_2$	5.979	5.551	0.928	2.676	2.396	0.289
$CdSiP_2$	5.728	5.289	0.923	2.584	2.271	0.296
$CdSnAs_2$	6.218	6.103	0.981	2.688	2.664	0.253
$CdSnP_2$	5.983	5.862	0.980	2.597	2.550	0.257
$MgGeAs_2$	6.020	5.638	0.936	2.637	2.473	0.273
$MgGeP_2$	5.796	5.365	0.926	2.551	2.355	0.279
$MgSiAs_2$	5.968	5.410	0.906	2.638	2.385	0.286
$MgSiP_2$	5.746	5.125	0.892	2.555	2.265	0.292
$MgSnAs_2$	6.152	6.042	0.982	2.642	2.654	0.248
$MgSnP_2$	5.935	5.799	0.977	2.558	2.543	0.252
$ZnGeP_2$	5.500	5.420	0.985	2.383	2.357	0.254
$ZnSiAs_2$	5.676	5.530	0.974	2.480	2.395	0.263
$ZnSiP_2$	5.420	5.268	0.972	2.383	2.270	0.268
$ZnSnAs_2$	5.944	5.961	1.003	2.498	2.659	0.226
$ZnSiP_2$	5.703	5.718	1.003	2.402	2.545	0.228

TABLE II. High-frequency macroscopic static dielectric constants or ion-clamped static (optical) dielectric constant or electronic dielectric constant (ε_∞), screening parameters (μ in bohr $^{-1}$), and direct KS band gaps (in eV) using PBE, DDH, and HSE06. Here RPA@DDH is evaluated using the scheme given in Fig. 1. The PBE, DDH, and HSE06 band gaps are corrected for spin-orbit coupling (SOC). Error statistics in band gaps with respect to experimental values are also given. The experimental reference values of I-III-VI_2 and II-IV-V_2 are taken from Refs. [92] and [68], respectively. Here, the "−" lines indicate that those systems are treated as metals when using PBE. The band-gap values close to the experiment one are in bold font. Total ME (in eV), MAE (in eV), and MARE are also shown at the end of the table.

Solids	ε_∞ (RPA@PBE)	ε_∞ (RPA@DDH)	$\mu = \mu_{\text{eff}}^{\text{fit}}$	E_g (PBE)	E_g (DDH)	E_g (HSE06)	E_g (GW_0)	E_g (Expt.)	Δ_{SOC}[a]
					I-III-VI_2				
$AgAlS_2$	5.46	4.97	0.78	1.86	**3.70**	3.05	3.32[b]	3.60	0.00
$AgAlSe_2$	6.64	5.70	0.78	1.07	2.67	2.18	**2.43**[b]	2.55	0.03
$AgAlTe_2$	8.30	7.30	0.73	0.86	1.88	1.98	**2.16**[b]	2.30	0.17
$AgGaS_2$	6.65	5.38	0.82	1.11	**2.86**	2.30	2.16[b]	2.73	0.01
$AgGaSe_2$	8.85	6.18	0.82	0.51	**2.06**	1.62	1.29[b]	1.83	0.03
$AgGaTe_2$	15.39	8.78	0.79	0.13	1.19	**1.23**	1.17[b]	1.36	0.17
$AgInS_2$	7.56	5.21	0.74	0.49	2.23	**1.57**	1.32[b]	1.87	0.01
$AgInSe_2$	–	6.09	0.74	0.02	**1.56**	1.06	0.73[b]	1.24	0.04
$AgInTe_2$	11.8	7.68	0.70	0.18	1.28	1.34	**0.81**[b]	1.04	0.19
$CuAlS_2$	6.23	5.20	0.78	1.66	3.87	**3.20**	2.96[b]	3.46	0.01
$CuAlSe_2$	7.73	6.05	0.78	0.84	**2.76**	2.32	2.13[b]	2.65	0.02
$CuAlTe_2$	9.42	7.85	0.75	0.93	1.96	**2.01**	1.85[b]	2.06	0.09
$CuGaS_2$	7.80	5.55	0.70	0.89	3.17	2.22	1.68[d], 1.78[b], **2.35**[e]	2.50	0.01
$CuGaSe_2$	13.57	6.42	0.70	0.27	2.33	1.55	0.93[d], 0.99[b], **1.60**[e]	1.67	0.04
$CuGaTe_2$	12.54	8.54	0.66	0.36	**1.45**	1.65	0.90[b]	1.25	0.18
$CuInS_2$	–	5.98	0.73	0.03	1.72	1.03	0.77[d], 0.69[b], **1.41**[e]	1.55	−0.03
$CuInSe_2$	17.41	6.70	0.73	0.01	1.48	0.88	0.46[b], **0.93**[e]	1.04	0 .01
$CuInTe_2$	–	9.05	0.71	0.01	**1.14**	1.17	0.70[b]	1.00	0.17
					II-IV-V_2				
$BeGeAs_2$	11.30	10.47	0.81	0.55	**1.31**	1.30	1.07[c]	1.68	0.07
$BeGeP_2$	9.33	8.81	0.85	0.87	1.61	**1.54**	1.58[c]	0.90	−0.01
$BeSiAs_2$	9.76	9.32	0.82	0.97	1.82	1.79	**1.33**[c]	1.11	0.09
$BeSiP_2$	8.63	8.37	0.86	1.18	1.95	1.90	**1.75**[c]	1.30	0.03
$BeSnAs_2$	11.52	10.79	0.79	0.56	1.32	1.34	**1.25**[c]	1.15	0.11
$BeSnP_2$	9.57	9.23	0.82	0.88	1.60	1.57	**1.78**[c]	1.98	0.03
$CdGeAs_2$	25.26	12.92	0.74	0.11	**0.43**	0.17	0.26[c]	0.57	0.04
$CdGeP_2$	11.45	9.55	0.78	0.63	1.39	1.38	**1.61**[c]	1.72	0.00
$CdSiAs_2$	15.30	10.64	0.76	0.33	1.12	1.19	**1.29**[c]	1.55	0.04
$CdSiP_2$	9.55	8.94	0.81	1.42	**2.09**	2.06	1.91[c]	2.20	0.00
$CdSnAs_2$	13.24	4.03	0.71	0.07	**0.18**	0.03	0.16[c]	0.26	0.03
$CdSnP_2$	18.53	9.34	0.74	0.24	0.97	0.98	**1.10**[c]	1.17	0.02
$MgGeAs_2$	11.54	9.31	0.72	0.49	**1.34**	1.26	1.27[c]	1.60	0.05
$MgGeP_2$	8.48	7.75	0.75	1.52	2.26	**2.15**	2.28[c]	2.17	−0.03
$MgSiAs_2$	9.14	8.47	0.74	1.21	**2.02**	1.91	1.40[c]	2.00	0.04
$MgSiP_2$	7.79	7.42	0.77	1.37	**2.18**	2.03	1.83[c]	2.26	0.00
$MgSnAs_2$	12.13	9.02	0.69	0.31	**1.17**	1.10	1.07[c]	1.20	0.07
$MgSnP_2$	8.21	7.52	0.72	1.18	2.02	1.93	**2.05**[c]	2.48	0.00
$ZnGeAs_2$	–	11.59	0.77	0.06	**0.72**	0.65	0.67[c]	1.15	0.01
$ZnGeP_2$	10.47	9.24	0.81	1.14	1.97	**1.91**	2.25[c]	1.80	0.01
$ZnSiAs_2$	11.59	10.16	0.79	0.81	**1.76**	1.79	1.94[c]	1.60	0.05
$ZnSiP_2$	9.34	8.68	0.83	1.35	**2.09**	2.04	1.92[c]	2.30	0.01
$ZnSnAs_2$	–	11.69	0.74	0.00	**0.46**	0.44	0.44[c]	0.75	0.00
$ZnSiP_2$	10.45	8.68	0.83	1.35	**2.09**	1.48	1.92[c]	2.30	0.01
TME				0.95	**0.02**	0.15	0.17		
TMAE				0.95	**0.24**	0.27	0.28		
TMARE				0.57	**0.17**	0.20	0.19		

[a]Spin-orbit coupling is defined as $\Delta_{\text{SOC}} = E_g^{\text{PBE}} - E_g^{\text{PBE-SOC}}$, which has been added with all SOC uncorrected band gaps obtained from DFT calculations.

[b]Present work calculated with GW_0 from VASP. See main text for details.

[c]GW_0 values from Ref. [68]. These calculations are performed using the VASP code.

[d]G_0W_0@PBE from Ref. [20].

[e]G_0W_0@PBE+U from Ref. [20].

2. Calculation details

The density functional calculations are performed using the plane-wave formalism as implemented in the Vienna Ab initio Simulation Package (VASP) code [70–73]. A kinetic energy cutoff of 520 eV is used for all DFT calculations. We use a Monkhorst-Pack (MP) -like Γ-centered 11×11×11 **k**-points mesh to sample the Brillouin zone (BZ) for PBE calculations, whereas for DDH and HSE06, the **k**-points are reduced to 8×8×8. The electronic energies are allowed to converge at 10^{-6} eV for all DFT methods to achieve self-consistency. The relaxation of the structures is performed until the Hellmann-Feynman forces on atoms are reduced to less than 0.01 eV/Å^{-1}. The VASP-recommended projector augmented wave (PAW) pseudopotentials are used. Noteworthy, relatively deep Ga 3*d*, Ge 3*d*, and In 4*d*, states are treated as valence orbitals.

We also perform partially self-consistent quasiparticle GW_0 calculations from the VASP code whenever required for band gaps. The implementation of this method in VASP is described in Ref. [67]. For the quasiparticle calculations, the number of virtual orbitals is increased to 240 (using NBANDS = 240), and four iterations for the self-consistent GW_0 steps are used (using NELMGW = 4) after G_0W_0 calculation. The VASP-recommended *GW* pseudopotentials are used, where relatively deep Ga 3*d*, Ge 3*d*, and In 4*d* states are treated as valence orbitals. 8×8×8 Γ-centered *k* points are used to sample the Brillouin zone in GW_0 calculations. For all our cases, the starting point of many-body perturbation theory is the GGA PBE functional.

The optical absorption spectrum for DDH and HSE06 is also performed using the VASP code with 16×16×16 MP-like Γ-centered **k**-points with 72 empty orbitals. We have performed the DDH and HSE06 calculations in many shifted 4×4×4 **k**-points and weight over the multiple grids, as a straightforward calculation of hybrids would be expensive [74].

B. Self-consistent screened-DDH calculation

The central quantity of the screened DDH is to determine high-frequency macroscopic static dielectric constants, the ion-clamped static (optical) dielectric constant, or the electronic dielectric constant, ε_∞, and the screening parameter, μ. As mentioned before, in our case we use $\mu = \mu_{\text{eff}}^{\text{fit}}$ of Eq. (8). The calculations of $\mu_{\text{eff}}^{\text{fit}}$ are done using the local density approximation (LDA) densities, and they are also used for all the chalcopyrite systems. These values are supplied in Table II. As shown in Table II, $\mu_{\text{eff}}^{\text{fit}}$'s remain almost constants to a typical average value 0.72 bohr^{-1}, although for a few systems their value becomes ∼0.80 Bohr^{-1}. These values are consistent with the earlier reported values for common semiconductors and insulators [23,26]. Note that in Ref. [23], μ's are calculated from the least-squares fitting to the dielectric function in the long-wavelength limit obtained from higher-level accurate calculations, such as random phase approximation (RPA) calculated using PBE orbitals (RPA@PBE) or using nanoquanta kernel and partially self-consistent *GW* calculations [67].

Next, we turn to the calculations of the static dielectric constant, which is the central quantity for any DDH. As for our present case, we already fixed the μ to $\mu_{\text{eff}}^{\text{fit}}$ from the scheme

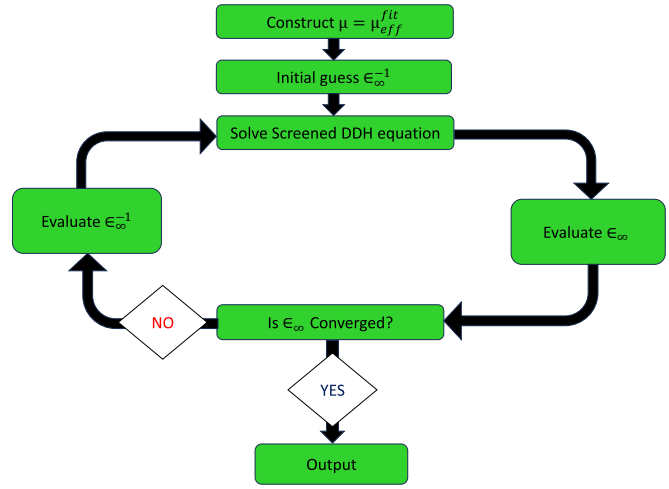

FIG. 1. Pictorial representation of the self-consistency of the screened DDH functional used in this paper.

described above. Considering ε_∞, it can be calculated using various schemes: (i) density functional perturbation theory (DFPT) within the framework of the RPA [82], or (ii) using the modern theory of polarization [83,84].

The fundamental equation that has been solved to calculate the dielectric tensor for bulk solid is

$$\varepsilon_{\mathbf{G},\mathbf{G}'}(\mathbf{q},\omega) = \delta_{\mathbf{G},\mathbf{G}'} - \frac{4\pi}{|\mathbf{G}+\mathbf{q}||\mathbf{G}'+\mathbf{q}|}\chi_{\mathbf{G},\mathbf{G}'}(\mathbf{q},\omega). \quad (11)$$

Our interest lies in the inverse of the macroscopic dielectric matrix $\varepsilon_\infty^{-1}(\mathbf{q},\omega)$, which is obtained from the head of the inversion of the full microscopic dielectric tensor as

$$\varepsilon_\infty^{-1}(\mathbf{q},\omega) = \lim_{\mathbf{q}\to 0}\varepsilon_{0,0}^{-1}(\mathbf{q},\omega). \quad (12)$$

In Eq. (11), the reducible polarizability $\chi_{\mathbf{G},\mathbf{G}'}(\mathbf{q},\omega)$ is defined as

$$\chi_{\mathbf{G},\mathbf{G}'} = \chi^0_{\mathbf{G},\mathbf{G}'} + \chi^0_{\mathbf{G},\mathbf{G}'}\Big(\frac{4\pi}{|\mathbf{G}+\mathbf{q}||\mathbf{G}'+\mathbf{q}|} + f_{\text{xc}}(\mathbf{q},\omega)\Big)\chi_{\mathbf{G},\mathbf{G}'}, \quad (13)$$

where $\chi^0_{\mathbf{G},\mathbf{G}'}(\mathbf{q},\omega)$ is the irreducible polarizability matrix obtained from KS systems [85–87], and $f_{\text{xc}}(\mathbf{q},\omega)$ is the XC kernel, obtained from the derivative of the exchange-correlation potential [82]. However, $f_{\text{xc}}(\mathbf{q},\omega)$ can be neglected, as its inclusion in the polarizability calculation is observed to be negligible [88]. Henceforth, in this work the $\chi_{\mathbf{G},\mathbf{G}'}$ and dielectric constants are evaluated by neglecting $f_{\text{xc}}(\mathbf{q},\omega)$, i.e., within RPAs. Note that by using Bloch notation, one can write $\chi^0_{\mathbf{G},\mathbf{G}'}(\mathbf{q},\omega)$ in terms of the KS orbitals and energies [85,89,90]. Therefore, the evaluation of $\varepsilon_\infty(\mathbf{q},\omega)$ depends strongly on the choices of the XC functionals. Here, we perform RPA calculations of Eq. (11) with PBE orbitals (named RPA@PBE) and DDH orbitals (named RPA@DDH).

Finally, the self-consistent cycle to calculate the static $\varepsilon_\infty(\mathbf{q}\to\mathbf{0},\omega\to 0)$ using screened-DDH is described in Fig. 1. We conform to the following steps: (i) First, we calculate $\mu_{\text{eff}}^{\text{fit}}$ using Eq. (8) with LDA orbitals; (ii) second, we start with $\varepsilon_\infty(\mathbf{q}\to\mathbf{0},\omega\to 0)$ as obtained from PBE functional (RPA@PBE), and we plug it in our DDH expression Eq. (6)

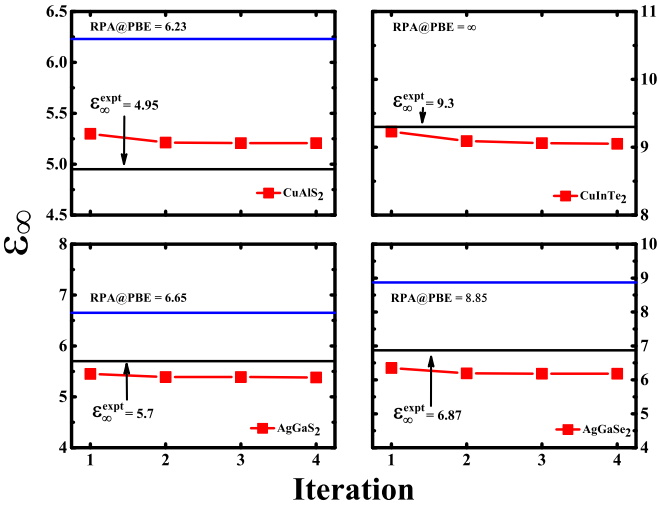

FIG. 2. Convergence of ε_∞ as obtained using RPA@DDH using the self-consistent cycle of Fig. 1. See Fig. 3 for the experimental values.

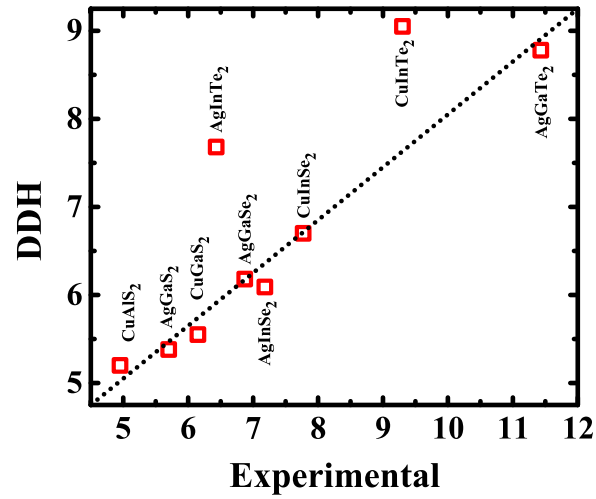

FIG. 3. The orientationally averaged static dielectric constants (optical), ε_∞, from experimental and RPA@DDH for nine Cu- and Ag-based chalcopyrites. The self-consistent cycle of Fig. 1 is used for RPA@DDH. The experimental values are used 7.77 for $CuInSe_2$ [75], 9.30 for $CuInTe_2$ [76], 6.15 for $CuGaS_2$ [77], 4.95 for $CuAlS_2$ [78], 7.18 for $AgInSe_2$ [79], 6.43 for $AgInTe_2$ [79], 6.87 for $AgGaSe_2$ [80], 5.70 for $AgGaS_2$ [81], and 11.43 for $AgGaTe_2$ [80].

along with previously calculated $\mu_{\text{eff}}^{\text{fit}}$; and (iii) third, we perform the DDH calculation and update $\varepsilon_\infty(\mathbf{q} \to \mathbf{0}, \omega \to 0)$ as obtained from RPA@DDH as long as the self-consistency in $\varepsilon_\infty(\mathbf{q} \to \mathbf{0}, \omega \to 0)$ is reached. In Fig. 2 we illustrate the self-consistency of $\varepsilon_\infty(\mathbf{q} \to \mathbf{0}, \omega \to 0)$ using RPA@DDH using the scheme of Fig. 1. The self-consistency of $\varepsilon_\infty(\mathbf{q} \to \mathbf{0}, \omega \to 0)$ is achieved mostly within four cycles. It is worth mentioning that for certain chalcopyrites, the PBE predicts a metallic nature with zero band gaps, leading to $\varepsilon_\infty(\mathbf{q} \to \mathbf{0}, \omega \to 0) \to \infty$ at RPA@PBE. In such cases, one needs to initiate the self-consistency process illustrated in Fig. 1 from a finite value of $\varepsilon_\infty(\mathbf{q} \to \mathbf{0}, \omega \to 0)$. Note that the potential is solved in all materials using the gKS scheme [91].

C. High-frequency dielectric constants

In Table II, we first calculate the orientationally averaged ε_∞ (i.e., $\varepsilon_\infty = \frac{\varepsilon_\infty^{xx}+\varepsilon_\infty^{yy}+\varepsilon_\infty^{zz}}{3}$) with RPA using PBE and DDH XC approximations with μ using Eq. (8). The analysis from Table II reveals that, for I-III-VI2, RPA@PBE tends to overestimate $\varepsilon\infty$ compared to RPA@DDH. Notably, for several cases such as $AgGaTe_2$, $AgInTe_2$, $CuGaSe_2$, $CuInS_2$, $CuGaTe_2$, and $CuInTe_2$, RPA@PBE predicts significantly large $\varepsilon\infty$, particularly when PBE incorrectly predicts a metallic structure. The dielectric constants calculated with RPA@PBE show inaccuracies for such materials. A similar trend is observed for II-IV-V_2 chalcopyrite semiconductors. However, in cases such as $ZnGeAs_2$ and $ZnSnAs_2$, PBE calculations lead to a metallic outcome. Across all instances, there is a noticeable magnitude difference of approximately ∼2 when comparing RPA@DDH and RPA@PBE. Examining the ε_∞ values from RPA@DDH, we observe that all values are finite and fall within the range expected for an ideal chalcopyrite semiconductor. This performance highlights the inadequacy of RPA@PBE in accurately calculating ε_∞ for these systems.

Next, Fig. 3 provides a comparison of ε_∞ for 11 Cu- and Ag-based chalcopyrites obtained from RPA@DDH and experimental data derived from optical reflectivity experiments (refer to the references in the caption of Fig. 3). We observe a remarkable agreement between the calculated $\varepsilon_\infty^{\text{RPA@DDH}}$ and the experimental results. Conversely, for most of these systems, PBE-predicted ε_∞ values are quite large, with most systems exhibiting metallic behavior (as shown in Table II).

Finally, in Fig. 4 we compare the model dielectric function described by Eq. (7) (with $\alpha = 1$, $\mu = \mu_{\text{eff}}^{\text{fit}}$, and self-consistent ε_∞^{-1} evaluated at RPA@DDH, as per Table II) with the dielectric function obtained through G_0W_0 or RPA calculations for various chalcopyrite semiconductors. The details

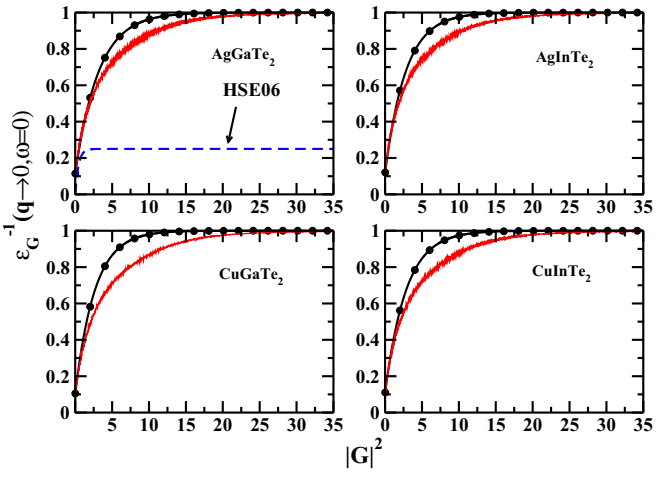

FIG. 4. Comparison of model dielectric function as a function of **G** (in Bohr^{-1}) for four chalcopyrite semiconductors. The black circle line indicates the model function with parameters evaluated at RPA@DDH (see Table II), whereas the red line corresponds to the G_0W_0 or RPA calculations.

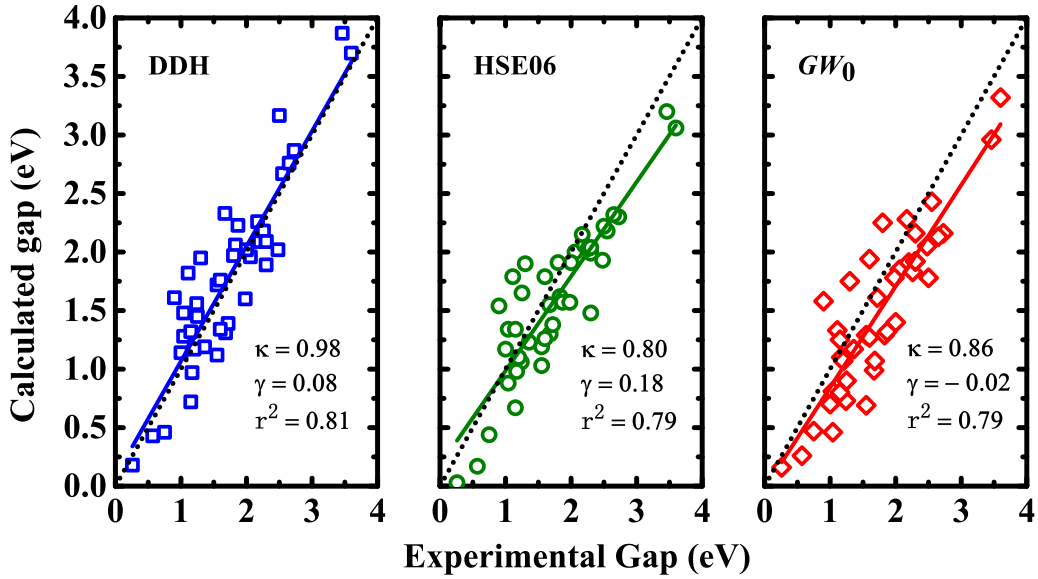

FIG. 5. The calculated vs experimental band gaps of 42 chalcopyrite semiconductor using DDH, HSE06, and GW_0. The linear regressions formula is defined as $E_g^{calc} = \kappa E_g^{expt} + \gamma$, where κ is the slope, γ is the intercept (in eV), and r^2 is the correlation coefficient. The dashed lines in every panel give $E_g^{calc} = E_g^{expt}$. For GW_0, use the best value from Table II.

of the calculation procedure can be found in Ref. [74]. This comparison illustrates that the model dielectric function given by Eq. (7) aligns well with dielectric functions calculated through *ab initio* methods.

D. Analysis of band structures

1. Band gaps and band structures

Now, let us delve into the performance of DDH in estimating the band gaps. Table II provides a comprehensive comparison by presenting (g)KS band gaps obtained from PBE, HSE06, and GW_0. The band gap is defined as $E_g = \varepsilon_{LUMO} - \varepsilon_{HOMO}$, where ε_{LUMO} and ε_{HOMO} represent the corresponding lowest unoccupied molecular orbital (LUMO) and highest occupied molecular orbital (HOMO) eigenvalues.

Inspecting the band gaps of I-II-VI_2, one can readily observe that, as usual, PBE underestimates the band gaps for all systems and becomes zero for $AgGaTe_2$, $AgInTe_2$, $CuGaSe_2$, $CuGaTe_2$, and $CuInS_2$. Although HSE06 offers an improvement over PBE, an important improvement is observed in DDH calculations. Using DDH, the band gap increases to ~ 0.8 eV for Ag-based chalcopyrites compared to HSE06, making DDH band gaps close to the experimental values. Similarly, for Cu-based chalcopyrites, the gaps obtained using DDH are also in good agreement. We observe good performance for $CuAlSe_2$, $CuGaTe_2$, and $CuInTe_2$ using DDH, which brings it closer to experimental values. One may note that for Cu-based chalcopyrites, the interplay between Cu d and anions p is identified as a crucial factor [9,20,21]. Interestingly, for $CuGaS_2$, $CuGaSe_2$, $CuInS_2$, and $CuInSe_2$, the underestimation in the band gap from G_0W_0 and GW_0 is noticeable. As mentioned in Ref. [68], the screening is not treated correctly by G_0W_0, and the PBE+U method may be the better starting point for quasiparticle GW calculations [9,20,21]. For example, using the PBE+U as a starting point for G_0W_0, the band gaps of $CuInS_2$ improve to 1.41 eV, where the G_0W_0@PBE value was 0.77 eV (in our present calculation, it is 0.69 for GW_0, which is close to the G_0W_0@PBE value of Ref. [20]). A similar improvement in results is also noticed when employing PBE+U as a starting point for Cu-based chalcopyrite semiconductors. In accordance with the insights from Ref. [9], these systems call for careful treatment of GW, requiring fully self-consistent (sc)COHSEX or GW for precise band-gap predictions. Nevertheless, the remarkable performance of DDH in these semiconductor materials hints at its potential to be the preferred method, offering a commendable balance between accuracy and relatively lower computational cost compared to the self-consistent GW. Similarly, DDH also delivers accurate results for II-IV-V_2 semiconductors and is closely aligned with the experimental values.

Figure 5 shows the experimental versus theoretical band gaps obtained using DDH, HSE06, and GW_0. We use linear regression analysis to understand better the errors coming from different methods. We calculate slope (κ), interception (γ), and correlation coefficient (r^2) for comparison. For DDH, the κ, γ, and correlation coefficient r^2 are found to be about 0.98, 0.08, and 0.81 which are slightly better than HSE06. Considering the GW_0, its error statistics are similar to HSE06. The most relevant parameter here is r^2, which is marginally better for DDH functional than HSE06 and GW_0. Also, as shown in Table II, in terms of total mean absolute error (MAE) and mean absolute relative error (MARE), DDH performs marginally better than HSE06 as well as GW_0.

In Fig. 6, we plot the band structures from PBE, HSE06, and DDH for $CuGaS_2$, a direct band gap (located at the Γ-point) semiconductor. We observe an identical band structure and curvature apart from the shift in the conduction band for different methods. Specifically, DDH shows a noticeable ~0.97 eV shift in the conduction band at the Γ-point compared to HSE06.

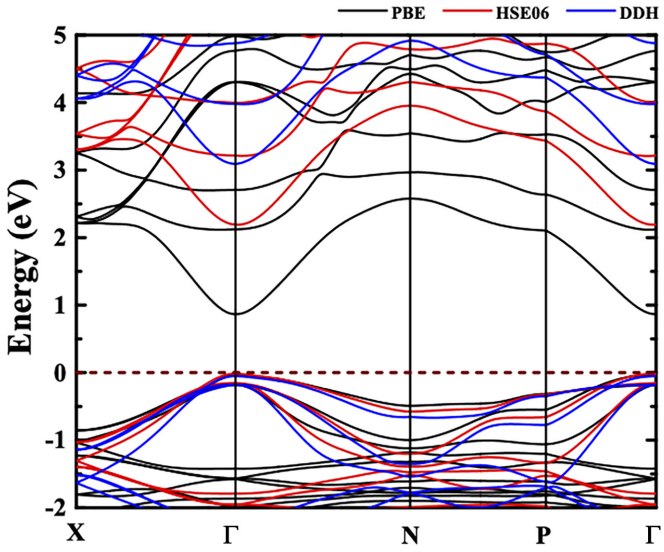

FIG. 6. Band structure of $CuGaS_2$ calculated using PBE, HSE06, and DDH. The dashed line indicates the Fermi energy.

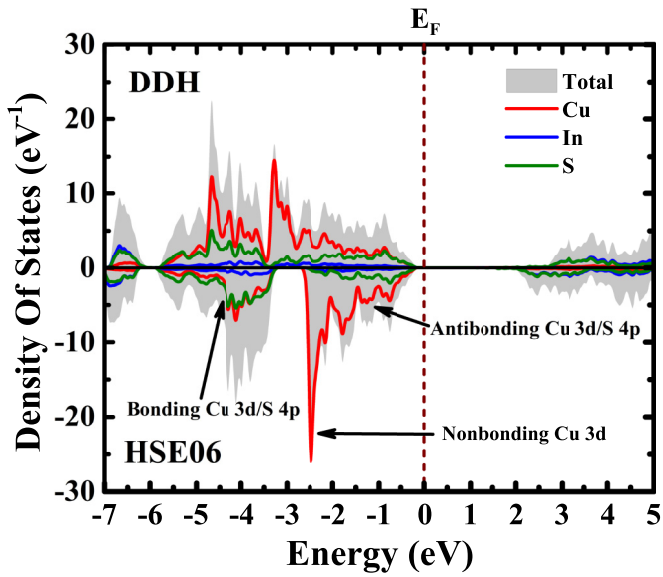

FIG. 8. Density of states (DOS) for $CuInS_2$ calculated using DDH and HSE06.

2. *Variation of band gaps with u*

To understand the variation of the band gaps with the distortion parameter "u" [defined in Eq. (10)], we show the band-gap variation of $CuInS_2$, one of the prototype chalcopyrite semiconductors, using various methods in Fig. 7. This is important because, experimentally, one can observe the stability of chalcopyrite with the variation of u. Typically, PBE predicts the system to be metallic for $0.20 \leqslant u \leqslant 0.215$. HSE06 improved over PBE but underestimated the band gap by ∼0.2 eV. A very similar performance is also observed from various sc-COHSEX+G_0W_0, while fully self-consistent sc-COHSEX improves over single-shot sc-COHSEX, i.e., sc-COHSEX+G_0W_0 [9]. In contrast, the improvements in the band gaps for DDH are quite noticeable over the ranges of u. Although DDH overestimates the band gaps only by ∼0.2 eV compared to the experimental values, it is well within the shaded part of Fig. 7. For each u, the DDH uses different Fock mixing by ε_∞^{-1}. The seemingly different band-gap values from different methods occur because of the different screening of these systems with various u, which is expected due to the interplay between u and the hybridization of the p-d orbitals [9].

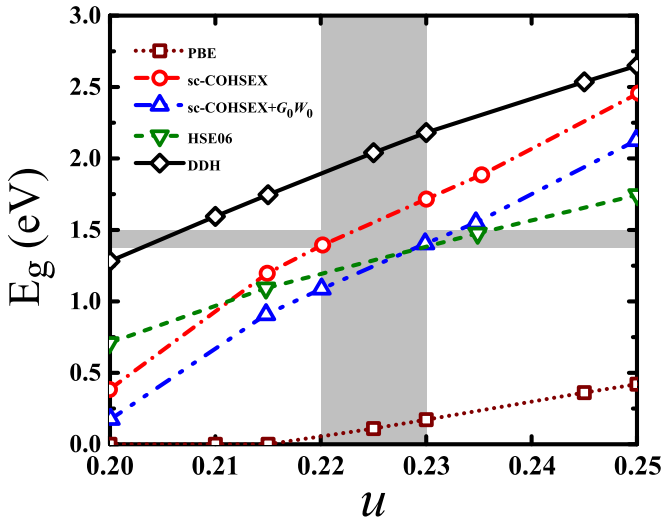

FIG. 7. Band gap vs the anion displacement u for $CuInS_2$ as obtained using different methods. The PBE, HSE06, sc-COHSEX, and sc-COHSEX+G_0W_0 values are taken from Ref. [9].

3. *Analysis of DOS and charge density*

More analysis can also be drawn from the density of states (DOS) for $CuInS_2$ in Fig. 8. Typically, the main contribution comes from metal Cu 3d, anion S 3p, and their (nonbonding/antibonding) hybridization. For DDH, there is a downward shift of nonbonding 3d states because of the stronger hybridization, which reduces the p-d repulsion, hence the enlargement of bandwidth.

The differences in the performances of DDH and HSE06 can also be drawn from the charge density contour plot of $CuInS_2$ as shown in Fig. 9. As known, the In − S bond is ionic, whereas the Cu − S bond is covalent. The nature of covalency changes due to the repulsive p-d nonbonding nature, which is depicted through the change density isosurface plot. The reduction in the isosurface value between Cu − S indicates a decrease of p-d repulsion in DDH; hence, the atomic distance becomes slightly lower than HSE06.

4. *Positions of valance d-bands*

Finally, in Table III, we show the mean positions of the occupied d band (in eV) (relative to the VBM) for several chalcopyrite semiconductors. As the PBE functional suffers from the known delocalization, its occupied d band is quite underestimated. Although HSE06 improves over PBE, DDH generally recovers the mean positions of the occupied d band quite remarkably compared to both HSE06 [26]. However, our results suggest nonempirical DDH obtains a bit of deep occupied d-band positions compared with GW_0. This is

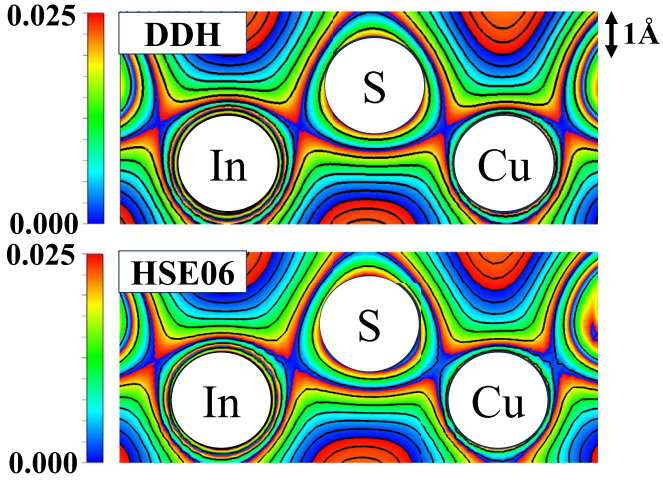

FIG. 9. Electronic charge-density distribution contours of $CuInS_2$ as obtained from DDH and HSE06. The positions of Cu, In, and S atoms are shown. The logarithmic scale is used for the better visualization of the isosurfaces.

because, for these systems, the band gaps are overestimated from DDH. Unfortunately, no experimental results are available with which to compare.

The analysis of band gaps, distortion parameter versus band-gap variations, the density of states, and the charge density indicate the screening effect as determined using DDH, which is important for determining accurate properties from hybrid functionals. Importantly, a judicious choice of the percentage of the Fock screening is required for a more accurate prediction of the properties. In that case, the functional becomes empirical or tuned DDH [33]. However, looking at the nonempirical settings and the superiority of the obtained properties, the present DDH can be considered as one of the useful methods, especially when higher-level accurate methods like *GW* are necessary but computationally unaffordable.

E. Optical bowing parameters

The band gap of ternary chalcopyrites varies from $CuBX_2$ to $AgBX_2$ due to the different sizes of Cu and Ag atoms. This variation is evident in Table II for all XC approximations. The band gap varies as the Cu/Ag ratio changes [93]. These size-dependent variations are further intensified

TABLE III. Mean positions of the occupied d band (in eV) relative to the VBM for selective semiconductors. The theoretical values are calculated by averaging the d-state energies at the Γ point.

Solids	PBE	DDH	HSE06	GW_0
$AgGaS_2$	−14.8	−19.8	−17.1	−17.3
$AgInS_2$	−14.4	−17.3	−15.9	−16.6
$AgInTe_2$	−14.8	−17.8	−16.4	−16.9
$AgGaTe_2$	−15.3	−20.4	−17.9	−16.7
$AgGaSe_2$	−14.9	−20.0	−17.3	−16.5
$CuGaS_2$	−15.4	−20.8	−17.6	−18.1
$CuInS_2$	−15.0	−17.7	−16.5	−17.0
$CuGaTe_2$	−15.4	−21.1	−17.9	−18.5

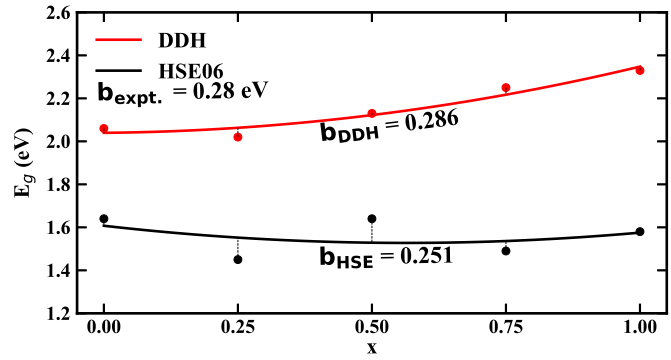

FIG. 10. The band-gap values for $Cu_xAg_{1-x}GaSe_2$ alloy are calculated at compositions $x = 0.0,\ 0.25,\ 0.50,\ 0.75,$ and 1.0, with DDH and HSE06. The curves are fitted using Eq. (14).

by band bowing, known as optical bowing [94]. This effect arises from atomic-level fluctuations in the lattice structure of (Cu,Ag)BX_2 compounds [95]. Due to level repulsion between chalcopyrite energy levels in the alloy, the band gap of the alloy experiences a downward shift from the linear average, as described by the following equation:

$$E_g(A_xB_{1-x}) = xE_g(A) + (1-x)E_g(B) - bx(1-x), \quad (14)$$

where $E_g(A)$ and $E_g(B)$ are the band gaps of A and B for the compound A_xB_{1-x}. Considering the quaternary chalcopyrite semiconductor alloy $Cu_xAg_{1-x}GaSe_2$, the common $Ga-X$ bond length remains almost unchanged with concentration x, while the $Ag-Se$ and $Cu-Se$ bond lengths associated with Ag and Cu increase with x [96]. This is consistent with the nearly identical Ga-Se bond lengths in $CuGaSe_2$ and $AgGaSe_2$ because the local environment of Ga does not change with the alloy concentration x. In the case of DDH, the band gap varies from 2.33 to 2.06 eV as we go from $CuGaSe_2$ to $AgGaSe_2$, and in the case of HSE06, it varies from 2.55 to 2.62, as shown in Table II. The optical bowing parameter "b" can be obtained using the band-gap difference. The band gaps for $Cu_xAg_{1-x}GaSe_2$ with concentrations of ($x = 0.0$, 0.25, 0.50, 0.75, 1.0) are calculated using PBE, DDH, and HSE06 XC approximations. The band-gap value using PBE for $x = 0.0$ and 0.25 is 0 eV, so PBE band-gap errors are largely canceled in the calculation. The optical bowing parameter "b" can be calculated at different x along with pure $AgGaSe_2$ and $CuGaSe_2$ according to Eq. (14).

Figure 10 is plotted by curve-fitting the calculated band gap using HSE06 and DDH using Eq. (14). The experimental value of "b" for $Cu_xAg_{1-x}GaSe_2$ is 0.280 eV [97]. The value of "b" using HSE06 is 0.251 eV, whereas for DDH it is 0.286 eV. Our study shows that the value of "b" using DDH is in very good agreement with the experimental optical bowing parameter compared to HSE06.

F. Description of absorption spectra

Optical-absorption properties of solids in DFT are mostly calculated using the linear-response TDDFT (LR-TDDFT) by solving the Casida equation using KS or gKS orbitals [100]. However, to get an accurate optical spectrum for a solid, it is necessary to get the correct band gap and accurate treatment

of the electrons and holes. State-of-the art BSE@*GW* includes the physics correctly but comes with huge computational expenses. Typically, in VASP, the excitation spectra for both the TDDFT and BSE@*GW* methods are calculated by solving the Casida/Bethe-Salpeter equation [19,100–103].

Within the Tamm-Dancoff approximation, the TDDFT spectrum is calculated by solving the matrix element of direct transition from occupied to unoccupied states and the electron-hole (*e-h*) interaction as [100–103]

$$A_{ij;ab} = \omega_{ia}\delta_{ij;ab} + \langle ib|K_{\mathrm{Hxc}}|aj\rangle, \tag{15}$$

where $\omega_{ia} = \varepsilon_i - \varepsilon_a$. The occupied states are denoted as i, j, unoccupied states are denoted as a, b, and corresponding KS or gKS eigenvalues are denoted by ε. The matrix element $\langle ib|K_{\mathrm{Hxc}}|aj\rangle$ is evaluated using the Hartree plus XC kernel, K_{Hxc}, which includes the *e-h* interaction. Because the semilocal functionals typically underestimate the band gaps, the first term on the right-hand side of Eq. (15), depending on the KS eigenvalues, is not well treated. The *e-h* interaction term is further simplified using the framework of the gKS and screened-DDH as Hartree and screened exchange, and the term involves the XC kernel as [103]

$$\begin{aligned}\langle ib|K_{\mathrm{Hxc}}|aj\rangle &= 2\langle ib|V(|\mathbf{q}+\mathbf{G}|)|aj\rangle \\ &\quad - \langle ib|f_{\mathrm{xc}}^{\mathrm{nonlocal}}|ja\rangle + \langle ib|f_{\mathrm{xc}}^{\mathrm{local}}|aj\rangle. \end{aligned}\tag{16}$$

The first term on the right side of the above matrix element involves the Hartree term that is common for both TDDFT and BSE@*GW*. The term involving $\langle ib|f_{xc}^{\mathrm{nonlocal}}|ja\rangle = \langle ib|\varepsilon_\infty^{-1}(|\mathbf{q}+\mathbf{G}|)V(|\mathbf{q}+\mathbf{G}|)|ja\rangle$ does not appear when considering only the semilocal XC functional. The local XC kernel, $f_{\mathrm{xc}}^{\mathrm{local}}$, is the functional derivative of semilocal XC approximations with respect to the density and does not include any excitonic effect. However, some specially designed low-cost XC kernels are also developed and include necessary features [104–111]. Importantly, for a short-range screened hybrid like HSE06, $\varepsilon_\infty^{-1}(|\mathbf{q}+\mathbf{G}|) = \beta(1 - e^{-|\mathbf{G}|^2/(4\mu)})$ and the resultant screened exchange varies as $\sim\beta$, a constant with $\beta = 0.25$ at $q \to 0$. However, for bulk systems, the correct behavior of screened exchange must be $\sim \frac{\varepsilon_\infty^{-1}(|\mathbf{G}|)}{q^2}$ at $q \to 0$, which is the key to improving the optical absorption spectra from DDH [34,88,112–119], where the high-frequency dielectric constant of the material replaces the dielectric function [103].

On the other hand, in BSE, the same set of equations are solved [19,103]. However, the orbitals are related to the previous *GW* calculations [19,103], typically obtained from different levels of approximations, where the screened exchange is frequency-dependent (through the dielectric function) [103] and the inclusion of the "nanoquanta" vertex correction may also be required for accurate calculations [67]. For the corresponding VASP implementation of the BSE equation and differences in the details of BSE and TDDFT using DDH, the readers are referred to Ref. [103]. While BSE calculations neglect dynamical effects, it is worth noting that determining the screened exchange in prior *GW* steps adds complexity to the overall problem [103].

Finally, in TDDFT, the frequency-dependent and small wave-vector limit of the imaginary $[\varepsilon_2(\omega)]$ part of the macroscopic dielectric function (optical), ε^M, is calculated via

$$\varepsilon_2(\omega) = \mathrm{Im}\{\lim_{q\to 0}\varepsilon^M(q,\omega)\}, \tag{17}$$

where $\lim_{q\to 0}\varepsilon^M(q,\omega)$ is given by Eq. (48) of Ref. [102], which is also related to the calculated matrix elements of Eq. (15) and how the kernels are evaluated. It is quite apparent that the results obtained from TDDFT using the semilocal only and hybrid DFT functionals give drastically different results.

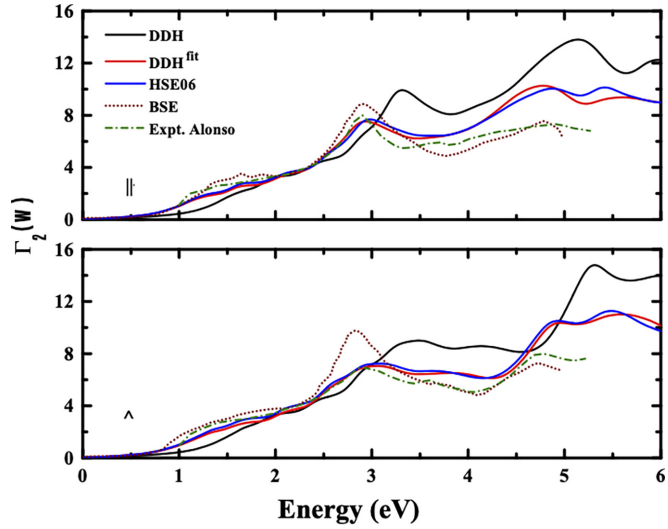

FIG. 11. Imaginary part of absorption spectra $[\varepsilon_2(\omega)]$ of $CuInSe_2$ (upper panel) for light polarized along the c axis (upper panel) and for light polarized perpendicular to the c axis (lower panel) calculated with DDH (nonempirical) and DDH$^{\mathrm{fit}}$ (with empirical tuning of parameter γ) and HSE06. The experimental and BSE@*GW* results are taken from Alonso *et al.* [6] and Korbel *et al.* [98], respectively.

In the following, we choose $CuInSe_2$ and $CuGaS_2$ to calculate the TDDFT spectrum, for which high-level calculations and experimental values are available. For $CuInSe_2$, we consider $a = 5.780$ Å, $c = 11.618$ Å, and $u = 0.230$ according to the experimental values in Table I of Ref. [120]. Similarly, for $CuGaS_2$ we choose $a = 5.351$ Å, $c = 10.478$ Å, and $u = 0.259$ according to the experimental values as supplied in Table II of Ref. [121]. To make a meaningful comparison, we compare the results from the KS (as obtained using DDH and HSE06) applying TDDFT, BSE solving the *GW* (BSE@*GW*), and the experimental dielectric functions. Figure 11 presents the absorption spectra for $CuInSe_2$ and Fig. 12 for $CuGaS_2$. In both cases, we show the spectra for the light-polarized perpendicularly to the c axis $([\varepsilon_2^{xx}(\omega) + \varepsilon_2^{yy}(\omega)]/2)$ or along the c axis $[\varepsilon_2^{zz}(\omega)]$.

Figure 11 compares the absorption onset of TDDDH, TDHSE06, BSE@*GW*, and experiment in the case of $CuInSe_2$. As is evident from the figure, a fairly good agreement of TDDDH with BSE@*GW* (BSE@*GW* spectrum is taken from Ref. [98]) and the experimental spectrum from Alonso *et al.* [6] is observed. Notably, excitonic peak positions obtained from TDDDH are at slightly higher energies or right-shifted when compared with the experimental and BSE@*GW* spectra. This is because of the overestimations in the orbital energies and hence the band-gap values from

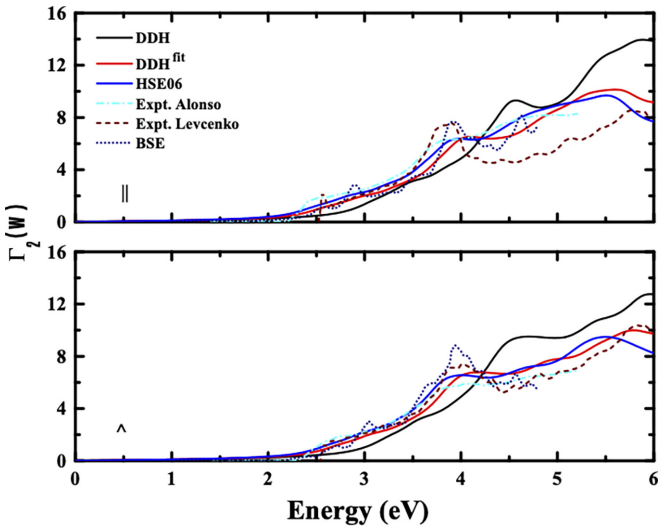

FIG. 12. Same as Fig. 11 but calculated for $CuGaS_2$. The experimental values are taken from Alonso *et al.* [6] and Levcenko *et al.* [99]. The BSE@*GW* results are taken from Aguilera *et al.* [21].

DDH [connected to the Casida Eq. (15)]. On the other hand, in the case of TDHSE06, we also observe good agreement with TDDDH. Note that the HSE06 absorption spectrum for these semiconductors is also reasonably good compared to the experimental spectrum. On the other hand, the advantage of TDDDH is that very accurate spectra can be obtained for both the semiconductor and insulators [26].

Very similar tendencies are obtained from TDDDH when compared for $CuGaS_2$. As shown in Ref. [21], for $CuGaS_2$ two absorption spectra are available from Alonso *et al.* [6] and Levcenko *et al.* [99]. We consider the experimental spectra of Alonso *et al.* [6], shown in Fig. 12, and those have better agreement with BSE spectra [21]. Considering TDDDH spectra, the first peak is higher energy than the experimental and BSE@*GW* spectra, as shown in Fig. 12. Regarding the TDHSE06, the excitonic peaks also agree with the experimental one, similar to the previous studies.

One can obtain a good absorption spectrum from TDDDH by empirically tuning the parameter γ of Eq. (4). Several other works have adopted this strategy [33,34,37,65]. The following strategies can be adopted to obtain a reasonable spectrum from TDDDH: (i) Tune parameter γ of Eq. (4) to match with the band gaps of G_0W_0 or GW_0 when no experimental band gap is available, or (ii) if experimental band gaps are available, then the tuning of the γ of Eq. (4) can be done to match with the experimental band gap of the system, keeping screening parameter μ fixed. Here, we consider the second strategy. After tuning γ from experimental band gaps, we compare the excitation spectrum with the BSE@*GW* or experimental spectrum. We obtain $\gamma = 0.08$ for $CuGaS_2$ and $\gamma = 0.06$ for $CuInSe_2$ to match the experimental band gaps. Consistent agreement is noted in absorption onsets, excitonic peak positions, and the higher-energy spectrum when compared to the spectrum for light polarized in both directions. Notably, the tuning procedure is usually not needed for systems in which DDH adequately describes band gaps.

IV. CONCLUSIONS

The comparative assessment of the screened-range-separated hybrids (such as HSE06), screened DDH, and methods based on the many-body perturbation theory are assessed for various properties of chalcopyrite semiconductors, such as band gaps, optical bowing parameters, and optical absorption spectrum. It is demonstrated that the screened DDH approach is not only promising as a cheaper alternative to many-body perturbation-theory-based approaches (such as G_0W_0 or *GW* and BSE@*GW*), but it is more flexible and physically sound than HSE06. The important fact is that in the screened DDH, the amount of screening correlation is determined from the static dielectric constant instead of a fixed screening used in HSE06. This makes the screened DDH more flexible, especially for the band gaps of chalcopyrites, where the amount of *p-d* hybridization is determined from screening correlation. Though the overall mean absolute error suggests that the band-gap performances of HSE06, screened DDH, and GW_0 (or G_0W_0) are quite similar, the screened DDH has a better overall slope, intercept, and correlation coefficient when compared with the experimental band gaps. We also observe that in Cu-based chalcopyrites, the accuracy of screened DDH for band gaps is slightly better than G_0W_0@PBE, which depends strongly on the initial starting point.

Also, a notable success of the TDDDH in the case of calculating the optical-absorption spectrum is demonstrated that is both cost-efficient and free from empiricism when compared with the BSE@*GW*. We hope that screened DDH can be the method of choice for evaluating the optical properties of chalcopyrite systems and different heterostructures where the BSE calculations are not feasible.

Finally, the overall quality performances of screened-DDH are encouraging as they are quite close to many-body perturbation calculations in providing the estimates of various properties. Importantly, the screened DDH is free of adjustable parameters (as opposed to HSE06). All the results are obtained by solving the generalized Kohn-Sham equation, and unlike the *GW* method, it involves no virtual orbitals. This makes the functional easy to use with minimum computational cost. The present study shows that this can be a method of choice for other chalcopyrite semiconductors, especially for Cu-based multinary semiconductors.

ACKNOWLEDGMENT

S.J. would like to thank Dr. Lucian A. Constantin for valuable comments, suggestions, and technical details.

[1] M. A. Green, Y. Hishikawa, E. D. Dunlop, D. H. Levi, J. Hohl-Ebinger, M. Yoshita, and A. W. Ho-Baillie, Progr. Photovolt.: Res. Appl. **27**, 3 (2019).

[2] P. Jackson, D. Hariskos, E. Lotter, S. Paetel, R. Wuerz, R. Menner, W. Wischmann, and M. Powalla, Progr. Photovolt.: Res. Appl. **19**, 894 (2011).

[3] A. Walsh, S. Chen, S.-H. Wei, and X.-G. Gong, Adv. Energy Mater. **2**, 400 (2012).

[4] W. Feng, D. Xiao, J. Ding, and Y. Yao, Phys. Rev. Lett. **106**, 016402 (2011).

[5] J. C. Rife, R. N. Dexter, P. M. Bridenbaugh, and B. W. Veal, Phys. Rev. B **16**, 4491 (1977).

[6] M. I. Alonso, K. Wakita, J. Pascual, M. Garriga, and N. Yamamoto, Phys. Rev. B **63**, 075203 (2001).

[7] T. Feurer, R. Carron, G. Torres Sevilla, F. Fu, S. Pisoni, Y. E. Romanyuk, S. Buecheler, and A. N. Tiwari, Adv. Energy Mater. **9**, 1901428 (2019).

[8] J. J. Plata, V. Posligua, A. M. Marquez, J. Fernandez Sanz, and R. Grau-Crespo, Chem. Mater. **34**, 2833 (2022).

[9] J. Vidal, S. Botti, P. Olsson, J.-F. Guillemoles, and L. Reining, Phys. Rev. Lett. **104**, 056401 (2010).

[10] S. Siebentritt, M. Igalson, C. Persson, and S. Lany, Progr. Photovolt.: Res. Appl. **18**, 390 (2010).

[11] J. L. Shay, B. Tell, H. M. Kasper, and L. M. Schiavone, Phys. Rev. B **5**, 5003 (1972).

[12] B. Tell, J. L. Shay, and H. M. Kasper, Phys. Rev. B **4**, 2463 (1971).

[13] C. Bellabarba, J. González, and C. Rincón, Phys. Rev. B **53**, 7792 (1996).

[14] L. Hedin, Phys. Rev. **139**, A796 (1965).

[15] F. Aryasetiawan and O. Gunnarsson, Rep. Prog. Phys. **61**, 237 (1998).

[16] E. E. Salpeter and H. A. Bethe, Phys. Rev. **84**, 1232 (1951).

[17] M. van Schilfgaarde, T. Kotani, and S. Faleev, Phys. Rev. Lett. **96**, 226402 (2006).

[18] T. Kotani, M. van Schilfgaarde, and S. V. Faleev, Phys. Rev. B **76**, 165106 (2007).

[19] G. Onida, L. Reining, and A. Rubio, Rev. Mod. Phys. **74**, 601 (2002).

[20] Y. Zhang, J. Zhang, W. Gao, T. A. Abtew, Y. Wang, P. Zhang, and W. Zhang, J. Chem. Phys. **139**, 184706 (2013).

[21] I. Aguilera, J. Vidal, P. Wahnón, L. Reining, and S. Botti, Phys. Rev. B **84**, 085145 (2011).

[22] N. P. Brawand, M. Vörös, M. Govoni, and G. Galli, Phys. Rev. X **6**, 041002 (2016).

[23] W. Chen, G. Miceli, G.-M. Rignanese, and A. Pasquarello, Phys. Rev. Mater. **2**, 073803 (2018).

[24] N. P. Brawand, M. Govoni, M. Vörös, and G. Galli, J. Chem. Theor. Comput. **13**, 3318 (2017).

[25] H. Zheng, M. Govoni, and G. Galli, Phys. Rev. Mater. **3**, 073803 (2019).

[26] S. Jana, A. Ghosh, L. A. Constantin, and P. Samal, Phys. Rev. B **108**, 045101 (2023).

[27] M. Gerosa, C. E. Bottani, L. Caramella, G. Onida, C. Di Valentin, and G. Pacchioni, J. Chem. Phys. **143**, 134702 (2015).

[28] M. Gerosa, C. E. Bottani, L. Caramella, G. Onida, C. Di Valentin, and G. Pacchioni, Phys. Rev. B **91**, 155201 (2015).

[29] G. Miceli, W. Chen, I. Reshetnyak, and A. Pasquarello, Phys. Rev. B **97**, 121112(R) (2018).

[30] M. Gerosa, C. E. Bottani, C. D. Valentin, G. Onida, and G. Pacchioni, J. Phys.: Condens. Matter **30**, 044003 (2018).

[31] Y. Hinuma, Y. Kumagai, I. Tanaka, and F. Oba, Phys. Rev. B **95**, 075302 (2017).

[32] P. Liu, C. Franchini, M. Marsman, and G. Kresse, J. Phys.: Condens. Matter **32**, 015502 (2020).

[33] G. Ohad, D. Wing, S. E. Gant, A. V. Cohen, J. B. Haber, F. Sagredo, M. R. Filip, J. B. Neaton, and L. Kronik, Phys. Rev. Mater. **6**, 104606 (2022).

[34] D. Wing, J. B. Haber, R. Noff, B. Barker, D. A. Egger, A. Ramasubramaniam, S. G. Louie, J. B. Neaton, and L. Kronik, Phys. Rev. Mater. **3**, 064603 (2019).

[35] A. Ramasubramaniam, D. Wing, and L. Kronik, Phys. Rev. Mater. **3**, 084007 (2019).

[36] L. Kronik and S. Kümmel, Adv. Mater. **30**, 1706560 (2018).

[37] M. Camarasa-Gómez, A. Ramasubramaniam, J. B. Neaton, and L. Kronik, Phys. Rev. Mater. **7**, 104001 (2023).

[38] S. Jana, A. Patra, and P. Samal, J. Chem. Phys. **149**, 044120 (2018).

[39] B. Patra, S. Jana, L. A. Constantin, and P. Samal, Phys. Rev. B **100**, 155140 (2019).

[40] S. Jana, S. K. Behera, S. Śmiga, L. A. Constantin, and P. Samal, New J. Phys. **23**, 063007 (2021).

[41] A. Patra, S. Jana, P. Samal, F. Tran, L. Kalantari, J. Doumont, and P. Blaha, J. Phys. Chem. C **125**, 11206 (2021).

[42] F. Tran, J. Doumont, L. Kalantari, P. Blaha, T. Rauch, P. Borlido, S. Botti, M. A. L. Marques, A. Patra, S. Jana *et al.*, J. Chem. Phys. **155**, 104103 (2021).

[43] A. Ghosh, S. Jana, T. Rauch, F. Tran, M. A. L. Marques, S. Botti, L. A. Constantin, M. K. Niranjan, and P. Samal, J. Chem. Phys. **157**, 124108 (2022).

[44] T. Lebeda, T. Aschebrock, J. Sun, L. Leppert, and S. Kümmel, Phys. Rev. Mater. **7**, 093803 (2023).

[45] J. P. Perdew and A. Zunger, Phys. Rev. B **23**, 5048 (1981).

[46] A. J. Cohen, P. Mori-Sánchez, and W. Yang, Chem. Rev. **112**, 289 (2012).

[47] P. Mori-Sánchez, A. J. Cohen, and W. Yang, Phys. Rev. Lett. **100**, 146401 (2008).

[48] S. Jana, B. Patra, H. Myneni, and P. Samal, Chem. Phys. Lett. **713**, 1 (2018).

[49] A. Ghosh, S. Jana, M. K. Niranjan, S. K. Behera, L. A. Constantin, and P. Samal, J. Phys.: Condens. Matter **34**, 075501 (2022).

[50] B. Patra, S. Jana, L. A. Constantin, and P. Samal, J. Phys. Chem. C **125**, 4284 (2021).

[51] A. Ghosh, S. Jana, M. K. Niranjan, F. Tran, D. Wimberger, P. Blaha, L. A. Constantin, and P. Samal, J. Phys. Chem. C **126**, 14650 (2022).

[52] J. P. Perdew, K. Burke, and M. Ernzerhof, Phys. Rev. Lett. **77**, 3865 (1996).

[53] J. Heyd, G. E. Scuseria, and M. Ernzerhof, J. Chem. Phys. **118**, 8207 (2003).

[54] A. V. Krukau, O. A. Vydrov, A. F. Izmaylov, and G. E. Scuseria, J. Chem. Phys. **125**, 224106 (2006).

[55] J. Heyd and G. E. Scuseria, J. Chem. Phys. **121**, 1187 (2004).

[56] S. Jana, A. Patra, L. A. Constantin, and P. Samal, J. Chem. Phys. **152**, 044111 (2020).

[57] S. Jana, B. Patra, S. Śmiga, L. A. Constantin, and P. Samal, Phys. Rev. B **102**, 155107 (2020).

[58] S. Jana, A. Patra, and P. Samal, J. Chem. Phys. **149**, 094105 (2018).

[59] S. Jana and P. Samal, Phys. Chem. Chem. Phys. **20**, 8999 (2018).

[60] S. Jana and P. Samal, Phys. Chem. Chem. Phys. **21**, 3002 (2019).

[61] Z.-H. Cui, Y.-C. Wang, M.-Y. Zhang, X. Xu, and H. Jiang, J. Phys. Chem. Lett. **9**, 2338 (2018).

[62] J. H. Skone, M. Govoni, and G. Galli, Phys. Rev. B **93**, 235106 (2016).

[63] J. Yang, S. Falletta, and A. Pasquarello, npj Comput. Mater. **9**, 108 (2023).

[64] A. Lorin, M. Gatti, L. Reining, and F. Sottile, Phys. Rev. B **104**, 235149 (2021).

[65] S. E. Gant, J. B. Haber, M. R. Filip, F. Sagredo, D. Wing, G. Ohad, L. Kronik, and J. B. Neaton, Phys. Rev. Mater. **6**, 053802 (2022).

[66] M. S. Hybertsen and S. G. Louie, Phys. Rev. B **34**, 5390 (1986).

[67] M. Shishkin, M. Marsman, and G. Kresse, Phys. Rev. Lett. **99**, 246403 (2007).

[68] V. L. Shaposhnikov, A. V. Krivosheeva, V. E. Borisenko, J.-L. Lazzari, and F. A. d'Avitaya, Phys. Rev. B **85**, 205201 (2012).

[69] J. E. Jaffe and A. Zunger, Phys. Rev. B **28**, 5822 (1983).

[70] G. Kresse and J. Hafner, Phys. Rev. B **47**, 558 (1993).

[71] G. Kresse and J. Furthmüller, Phys. Rev. B **54**, 11169 (1996).

[72] G. Kresse and D. Joubert, Phys. Rev. B **59**, 1758 (1999).

[73] G. Kresse and J. Furthmüller, Comput. Mater. Sci. **6**, 15 (1996).

[74] Improving the dielectric function-Vaspwiki—vasp.at, accessed 09-May-2023.

[75] H. Neumann, Sol. Cells **16**, 399 (1986).

[76] G. D. Holah, A. A. Schenk, S. Perkowitz, and R. D. Tomlinson, Phys. Rev. B **23**, 6288 (1981).

[77] J. Baars and W. Koschel, Solid State Commun. **11**, 1513 (1972).

[78] W. Koschel, V. Hohler, A. Räuber, and J. Baars, Solid State Commun. **13**, 1011 (1973).

[79] G. Kanellis and K. Kampa, J. Phys. France **38**, 833 (1977).

[80] O. Madelung, *Semiconductors. Other than Group IV Elements and III-V Compounds*, Data in Science and Technology (Springer-Verlag, Berlin, 1992).

[81] J. P. van der Ziel, A. E. Meixner, H. M. Kasper, and J. A. Ditzenberger, Phys. Rev. B **9**, 4286 (1974).

[82] S. Baroni, S. de Gironcoli, A. Dal Corso, and P. Giannozzi, Rev. Mod. Phys. **73**, 515 (2001).

[83] R. D. King-Smith and D. Vanderbilt, Phys. Rev. B **47**, 1651 (1993).

[84] R. Resta, Rev. Mod. Phys. **66**, 899 (1994).

[85] M. Gajdoš, K. Hummer, G. Kresse, J. Furthmüller, and F. Bechstedt, Phys. Rev. B **73**, 045112 (2006).

[86] R. W. Nunes and X. Gonze, Phys. Rev. B **63**, 155107 (2001).

[87] I. Souza, J. Íñiguez, and D. Vanderbilt, Phys. Rev. Lett. **89**, 117602 (2002).

[88] J. Paier, M. Marsman, and G. Kresse, Phys. Rev. B **78**, 121201(R) (2008).

[89] S. L. Adler, Phys. Rev. **126**, 413 (1962).

[90] N. Wiser, Phys. Rev. **129**, 62 (1963).

[91] R. Garrick, A. Natan, T. Gould, and L. Kronik, Phys. Rev. X **10**, 021040 (2020).

[92] H. Xiao, J. Tahir-Kheli, and W. A. I. Goddard, J. Phys. Chem. Lett. **2**, 212 (2011).

[93] A. Shaukat, J. Phys. Chem. Solids **51**, 1413 (1990).

[94] D. Mourad and G. Czycholl, Eur. Phys. J. B **85**, 153 (2012).

[95] A. Mudryi, I. Victorov, V. Gremenok, A. Patuk, I. Shakin, and M. Yakushev, Thin Solid Films **431-432**, 197 (2003).

[96] S.-H. Wei and A. Zunger, J. Appl. Phys. **78**, 3846 (1995).

[97] I.-H. Choi, S.-H. Eom, and P. Yu, J. Appl. Phys. **87**, 3815 (2000).

[98] S. Körbel, D. Kammerlander, R. Sarmiento-Pérez, C. Attaccalite, M. A. L. Marques, and S. Botti, Phys. Rev. B **91**, 075134 (2015).

[99] S. Levcenko, N. N. Syrbu, V. E. Tezlevan, E. Arushanov, S. Doka-Yamigno, T. Schedel-Niedrig, and M. C. Lux-Steiner, J. Phys.: Condens. Matter **19**, 456222 (2007).

[100] M. E. Casida, *Recent Advances in Density Functional Methods* (World Scientific, Singapore, 1995), pp. 155–192.

[101] T. Sander, E. Maggio, and G. Kresse, Phys. Rev. B **92**, 045209 (2015).

[102] T. Sander and G. Kresse, J. Chem. Phys. **146**, 064110 (2017).

[103] A. Tal, P. Liu, G. Kresse, and A. Pasquarello, Phys. Rev. Res. **2**, 032019(R) (2020).

[104] P. E. Trevisanutto, A. Terentjevs, L. A. Constantin, V. Olevano, and F. D. Sala, Phys. Rev. B **87**, 205143 (2013).

[105] A. V. Terentjev, L. A. Constantin, and J. M. Pitarke, Phys. Rev. B **98**, 085123 (2018).

[106] S. Sharma, J. K. Dewhurst, A. Sanna, and E. K. U. Gross, Phys. Rev. Lett. **107**, 186401 (2011).

[107] S. Rigamonti, S. Botti, V. Veniard, C. Draxl, L. Reining, and F. Sottile, Phys. Rev. Lett. **114**, 146402 (2015).

[108] M. van Faassen, P. L. de Boeij, R. van Leeuwen, J. A. Berger, and J. G. Snijders, Phys. Rev. Lett. **88**, 186401 (2002).

[109] S. Cavo, J. A. Berger, and P. Romaniello, Phys. Rev. B **101**, 115109 (2020).

[110] Y.-M. Byun and C. A. Ullrich, Phys. Rev. B **95**, 205136 (2017).

[111] Y.-M. Byun, J. Sun, and C. A. Ullrich, Electron. Struct. **2**, 023002 (2020).

[112] C. A. Ullrich, *Time-Dependent Density-Functional Theory: Concepts and Applications* (Oxford University Press, Oxford, New York, 2011).

[113] Z. H. Yang, F. Sottile, and C. A. Ullrich, Phys. Rev. B **92**, 035202 (2015).

[114] M. Städele, M. Moukara, J. A. Majewski, P. Vogl, and A. Görling, Phys. Rev. B **59**, 10031 (1999).

[115] M. Petersilka, U. J. Gossmann, and E. K. U. Gross, Phys. Rev. Lett. **76**, 1212 (1996).

[116] Y.-H. Kim and A. Görling, Phys. Rev. Lett. **89**, 096402 (2002).

[117] J. Sun and C. A. Ullrich, Phys. Rev. Mater. **4**, 095402 (2020).

[118] J. Sun, J. Yang, and C. A. Ullrich, Phys. Rev. Res. **2**, 013091 (2020).

[119] F. Kootstra, P. L. de Boeij, and J. G. Snijders, Phys. Rev. B **62**, 7071 (2000).

[120] N. Kim, P. P. Martin, A. A. Rockett, and E. Ertekin, Phys. Rev. B **93**, 165202 (2016).

[121] M. Han, Z. Zeng, T. Frauenheim, and P. Deák, Phys. Rev. B **96**, 165204 (2017).